



**HAL**  
open science

## Key Wavefront Sensors features for Laser-assisted Tomographic Adaptive Optics Systems on the ELT

Thierry Fusco, Guido Agapito, Benoit Neichel, Sylvain Oberti, Carlos Correia, Pierre Haguenauer, Cédric Plantet, Felipe Pedreros, Zibo Ke, Anne Costille, et al.

### ► To cite this version:

Thierry Fusco, Guido Agapito, Benoit Neichel, Sylvain Oberti, Carlos Correia, et al.. Key Wavefront Sensors features for Laser-assisted Tomographic Adaptive Optics Systems on the ELT. 2022. hal-03514231v1

**HAL Id: hal-03514231**

**<https://hal.science/hal-03514231v1>**

Preprint submitted on 6 Jan 2022 (v1), last revised 14 Sep 2022 (v2)

**HAL** is a multi-disciplinary open access archive for the deposit and dissemination of scientific research documents, whether they are published or not. The documents may come from teaching and research institutions in France or abroad, or from public or private research centers.

L'archive ouverte pluridisciplinaire **HAL**, est destinée au dépôt et à la diffusion de documents scientifiques de niveau recherche, publiés ou non, émanant des établissements d'enseignement et de recherche français ou étrangers, des laboratoires publics ou privés.

# Key Wavefront Sensors features for Laser-assisted Tomographic Adaptive Optics Systems on the ELT

Thierry Fusco<sup>a,b,†</sup>, Guido Agapito<sup>c,†</sup>, Benoit Neichel<sup>b</sup>, Sylvain Oberti<sup>d</sup>, Carlos Correia<sup>b</sup>, Pierre Haguenauer<sup>d</sup>, Cédric Plantet<sup>c</sup>, Felipe Pedreros<sup>b</sup>, Zibo Ke<sup>b</sup>, Anne Costille<sup>b</sup>, Pierre Jouve<sup>b</sup>, Lorenzo Busoni<sup>c</sup>, Simone Esposito<sup>c</sup>

<sup>a</sup>DOTA, ONERA, Université Paris Saclay (COMUE) [Châtillon]

<sup>b</sup>Aix Marseille Univ, CNRS, CNES, LAM, Marseille, France

<sup>c</sup>INAF, Arcetri Astrophysical Observatory, Largo E. Fermi 5, 50125-FIRENZE, Italy

<sup>d</sup>ESO, Karl-Schwarzschild-Str.2, 85748 Garching b. München, Germany

<sup>†</sup>co-first authors, Send all correspondence to thierry.fusco@onera.fr and guido.agapito@inaf.it

**Abstract.** Laser Guide Star [LGS] wave-front sensing [LGSWFS] is a key element of tomographic Adaptive Optics system. However, when considering Extremely Large Telescope [ELT] scales, the LGS spot elongation becomes so large that it challenges the standard recipes to design LGSWFS. For classical Shack-Hartmann Wave-Front Sensor [SHWFS], which is the current baseline for all ELT LGS-assisted instruments, a trade-off between the pupil spatial sampling (number of sub-apertures), the sub-aperture field-of-view and the pixel sampling within each sub-aperture is required. For ELT scales, this trade-off is also driven by strong technical constraints, especially concerning the available detectors and in particular their number of pixels. For SHWFS, a larger field of view per sub-aperture allows mitigating the LGS spot truncation, which represents a severe loss of performance due to measurement biases. For a given number of available detectors pixels, the sub-aperture Field of View [FoV] is competing with the proper sampling of the LGS spots, and/or the total number of sub-apertures. In this paper we propose a sensitivity analysis, and we explore how these parameters impacts the final performance. In particular we introduce the concept of super resolution, which allows to reduce the pupil sampling per WFS, and opens an opportunity to propose potential LGSWFS designs providing the best performance for ELT scales.

**Keywords:** adaptive optics, wavefront sensors, tomography, lasers, telescopes.

## 1 Introduction

Europe has just launched the construction of the largest ground-based telescope: the ELT <sup>(1)</sup>. In operation by 2027, this 40m giant will answer fundamental questions from the search for and characterization of planets to the formation and evolution of the first galaxies of the universe. Adaptive Optics (AO), by correcting in real time aberrations introduced by the atmosphere, is essential to reach the ultimate performances of this future facility. The ELT has therefore been designed as an adaptive telescope, which will provide images with an angular resolution of less than 10 milli-arcsec in the near infrared. For this purpose, the ELT is equipped with a deformable mirror in its optical train (the 4th mirror of the telescope, alias M4<sup>2</sup>), as well as 8 laser stations, <sup>1</sup> in order to create artificial sources (Laser Guide Stars or LGS) for wavefront analysis. Laser stars have been used in AO on 8/10m telescopes for about ten years now, and their performances are relatively well mastered. However, scaling up to a 40m telescope represents a much bigger challenge than a simple extrapolation of the current solutions, and new concepts are required, especially in the field of wavefront sensing.

In this work we focus on Shack-Hartmann WFS because it is currently the best suited WFS for LGS WFSensing. Although alternative solutions, like Pyramid <sup>(3)</sup> and Ingot WFS <sup>(4)</sup>, exist and are pursued actively <sup>(5,6)</sup>, they still have to be proved on sky and are therefore deemed not mature enough to be used within the ELT. Despite being a forced choice for LGS sensing, the SHWFS in

43 the context of ELT has a major downside as it requires a detector with a large number of pixels to  
44 satisfy at the same time the requirement on the extended spot sampling, both in term of pixel pitch  
45 and overall FoV, and on turbulence spatial sampling (7-9).

46 Although our work is general, it is particularly interesting for the tomographic adaptive optics  
47 systems of a couple of first light instruments of the ELT: MAORY<sup>10</sup> (Multi-conjugate Adaptive  
48 Optics RelaY) and HARMONI<sup>11</sup> (High Angular Resolution Monolithic Optical and Near-infrared  
49 Integral field spectrograph). We report in the following sections several examples derived from  
50 these instruments and the LGSWFS main parameters that we propose can be directly applied to  
51 them.

52 In this paper, we present the challenges of Laser-assisted tomography on ELT (Section 2),  
53 and the impact on the design of LGSWFS. Section 3 deals with a new concept, dubbed super-  
54 resolution, which allows to obtain good tomographic performance, with a reduced number of pupil  
55 sampling points. Section 4 deals with the specific application to the ELT case, in particular we  
56 analyse the impact of the sub-aperture size, of the spot sampling and truncation and of the noise  
57 propagation on the AO system performances. Finally, in Section 6 we report potential LGSWFS  
58 designs considering the performance sensitivities presented in the previous sections.

## 59 **2 Challenges of Laser-assisted tomographic AO on the ELT**

60 This section summarizes the main challenges imposed by the use of LGS for an ELT.

### 61 *2.1 Tip-Tilt information*

62 This is a well known problem for AO systems working with LGSs: the image motion (or Tip-Tilt  
63 modes) cannot be measured directly from the LGS itself.<sup>12</sup> The transition from 8m to 40m does  
64 not significantly change this fundamental limitation, and the LGS AO systems still require the use  
65 of a Natural Guide Star (NGS) to get these modes. Fortunately, we have some favorable factors  
66 for the determination of tip-tilt in the detection of wavefront error: (1) the isoplanatic angle of low  
67 order modes like tip-tilt is an order of magnitude larger than that of high order modes. And for an  
68 ELT, the outer scale of the turbulence can play a positive role in reducing the overall atmospheric  
69 Tip-Tilt energy. (2) The entire pupil of telescope can be used to measure the tip-tilt, and as a result,  
70 the NGS used for measuring Tip-Tilt only can be significantly fainter than the usual NGS stars in  
71 classical AO. Again, a full ELT pupil should allow to access fainter stars than an 8m telescope,  
72 hence potentially increasing the sky coverage. (3) The bandwidth of the close loop in terms of  
73 tip-tilt compensation is about 1/4 of that of the high order, which can be beneficial for increasing  
74 the integration time, hence improving the SNR on faint NGS. On the downside, one has to note  
75 that this is true for atmospheric tilt, but telescope vibrations or wind-shake, which becomes much  
76 stronger for an ELT, would still require a large measurement and control bandwidth. Note that  
77 the NGS performance estimation is provided in a companion paper (Plantet, Neichel et al. this  
78 review).

### 79 *2.2 Cone Effect*

80 The second main limitation of the laser guide star is the cone effect.<sup>13</sup> The laser is focused at finite  
81 altitude (somewhere in the middle of the Sodium layer), hence the wave we receive from the laser  
82 source is spherical. If an AO system can only use a single LGS beacon to sense the atmospheric  
83 turbulence, an error is made; this error is called cone effect or “Focus Anisoplanatism”. The larger

84 the diameter of the telescope, the more important the cone effect becomes. The mitigation to  
85 cone effect is to use more than a single LGS, and perform a tomographic reconstruction of the  
86 atmospheric volume above the telescope. This is further detailed in Section 3.

### 87 2.3 Spot elongation

88 The spot elongation comes from the fact that the laser stars are not point objects, but extended  
89 sources. Indeed, the layer of Sodium atoms, located at 90km above the telescope, has a thickness  
90 between 10km and 20km. The laser stars resulting from the excitation of these Sodium atoms by  
91 the laser light propagated from the telescope have thus a “cigar” shape in the Sodium layer. By  
92 perspective effect, they appear as extended objects (ellipses) on the opposite edge of the telescope  
93 pupil. For a 40m telescope, the laser spots have a size between 1arcsecond for those close to the  
94 Laser Launch Telescope (LLT) and a maximum expected elongation which can reach up to 25arc-  
95 seconds. The difficulty is therefore to perform a wave front analysis on highly extended objects,  
96 and whose elongation varies in the pupil. There has been several options proposed in the liter-  
97 ature to mitigate the spot elongation issue. The proposed solutions include modifications of the  
98 laser source itself, innovative wave-front sensing strategy and advanced centroiding algorithms.  
99 Of course these solutions are not exclusive, and a combination of some is possible.

100 The mitigation followed in this work is based on the work developed by Bechet et al.<sup>14</sup> The method  
101 consists in weighting the measurements in order to only reject the ones along the long axis of the  
102 elongation (truncated), while keeping those along the small axis (not truncated). For each spot,  
103 the gradient along the small axis would be kept, while the gradient along the long axis would be  
104 rejected if truncated. Thanks to the redundancy of the measurements, and thanks to the fact that in  
105 a side-launch configuration the elongated spots of one WFS correspond to the non-elongated spots  
106 of another WFS, the expected impact on performance should be small. This is detailed in Section 4.

107  
108 The above mentioned topic of LGS spot truncation naturally leads to a necessary trade-off  
109 between the LGS spot sampling and the total Field-of-View [FoV]. In fact, for a fixed number  
110 of pixels associated with a SHWFS, and a fixed number of sub-apertures, a potential solution to  
111 increase the FoV of each sub-aperture could be to increase the angular size of each pixel. Usually,  
112 the SHWFSs are designed to have a pixel size providing the Shannon sampling of the spots within  
113 each sub-aperture. For the LGS object, the smaller spot size that one can expect may be around  
114 1 arcsec FWHM. In this case, the ideal pixel size should be 0.5arcsec. Fixing the pixel size,  
115 and if the detector and number of subapertures are fixed, will automatically determine the FoV  
116 of the WFS. Increasing the pixel size can then be an option to increase the subaperture FoV and  
117 mitigate LGS truncation. However, working with larger pixels introduces an undersampling of  
118 the LGS spot, which induces non-linear effects (optical gains) in the centroid measurement. The  
119 extreme example would be working with quad-cells ( $2 \times 2$  pixels per subaperture), which are known  
120 to be very non-linear (<sup>15</sup>). Basically, when working with undersampled spots, the centroiding  
121 will become a function of the LGS spot size. For LGSWFS, and because the spot size changes  
122 across the pupil, the non-linearity will be different for each sub-aperture, making the wave-front  
123 reconstruction very complex. This dependence (known as optical gain for the pyramid WFS) has  
124 to be calibrated on-line, for example by dithering each LGS with a known signal (<sup>16</sup>). Even though  
125 this on-line calibration is feasible, it adds complexity to the AO system, and centroid gains remain

126 an additional error in the final performance of multi-LGS systems (<sup>17</sup>). This trade-off has been a  
127 key topic in the design and definition of the LGSWFSs for the ELT.

#### 128 *2.4 Key parameters for Laser WFSensing on the ELT*

129 As said above, several parameters will be impacting the final performance of the laser assisted AO  
130 system for the ELT. In the following we explore the performance sensitivity to several of these  
131 parameters. In particular, we investigate the following aspects:

- 132 • Pupil sampling (a.k.a. number of sub-apertures) and tomographic performance.
- 133 • LGS spot sampling vs. truncation trade-off.
- 134 • Noise propagation (flux and RON).

135 Note that in this work we aim at minimizing the sum of all the error terms (fitting, aliasing,  
136 noise, linearity and truncation) given the constraints of the available technology in terms of detec-  
137 tors. As we will show in the following sections, this bring the design in the direction of sub-optimal  
138 choice with respect to single issues like linearity and truncation. In fact, we could design WFSs  
139 that completely avoid these last two errors terms, but at the price of a lower overall performance.  
140 In the same way, using a large number of pixels per sub-aperture makes the noise larger, but it is  
141 the best overall solution to balance linearity and truncation errors.

142 Finally, note that in this work we do not focus on temporal error because the WFS characteris-  
143 tics we are interested in have no impact on it and, moreover, its weight in the overall error budget  
144 for first generation tomographic AO systems on the ELT is negligible with respect to the other  
145 terms presented here. In fact, it can be easily shown<sup>18</sup> that for the median atmospheric condition of  
146 Cerro Armazones<sup>19</sup> we expect a temporal error of about 50nm, much smaller than the error budget  
147 of HARMONI and MAORY (see Ref. 20, Plantet, Neichel et al. this review).

### 148 **3 Tomography and super-resolution**

149 Before detailing the optimization of the LGSWFS design for the ELT, we first introduce the concept  
150 of super-resolution,<sup>21,22</sup> and its application for tomographic AO systems.

151 On Wide-Field AO systems (either MCAO or LTAO) several WFSs sense the turbulence vol-  
152 ume to get a tomographic information of the disturbances above the telescope. This tomographic  
153 information can then be used to optimize the performance in a given direction (single DM →  
154 LTAO), or across a wider science FoV (several DM → MCAO). This configuration gives also an  
155 additional feature: the different lines of sight of the WFSs increase the number of measurements  
156 in the part of the metapupil illuminated by more than one laser. A few examples of the meta-pupil  
157 sampling of a tomographic system are shown in Fig. 1.

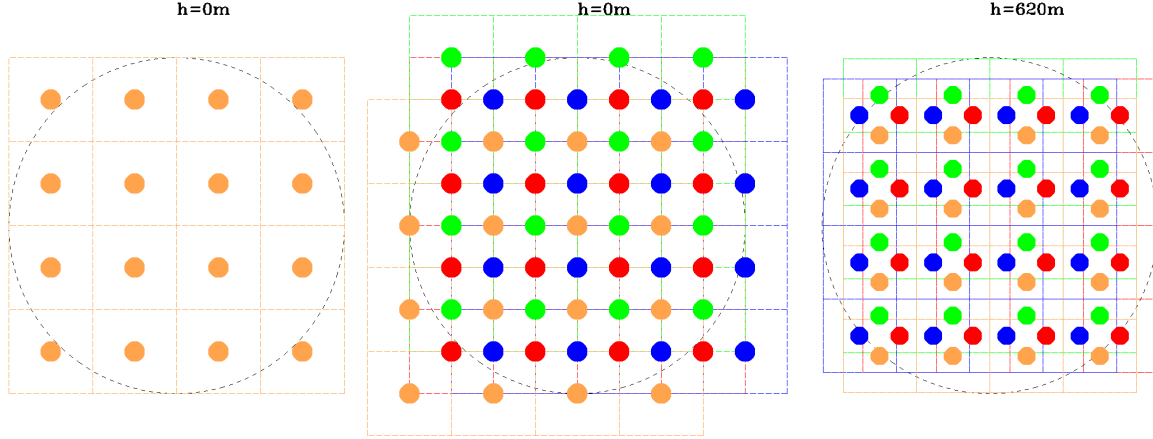


**Fig 1** Example of meta-pupil sampling with 4  $4 \times 4$  LGS WFSs with 50cm sub-apertures and an off-axis angle of 45arcsec. Different color are used to distinguish between the 4 WFSs. Left, altitude is 0m and no super-resolution is present because all sub-apertures are super imposed. Center, altitude is 0m and on purpose mis-alignments give a resolution of half the sub-aperture size. Right, altitude is 620m, the same of M4, and the sub-aperture shift coming from the 4 different line of sight,  $\alpha=45\text{arcsec}$ , give a naturally induced super-resolution that is approximately half the sub-aperture size.

158 Hence, we get information at an higher spatial frequency than the Nyquist's one given by  
 159 the number of sub-apertures of a single WFS. In other words, with multi LGS tomographic AO  
 160 system, the geometrical resolution is coming from free at least for the turbulent layers in altitude.  
 161 Unfortunately this free super-resolution is effective in a reduced altitude range because at ground  
 162 level all WFSs see the pupil with the same geometry and at high altitudes the sensed patch of the  
 163 WFS separates between each other. In particular the optimal shift of half sub-aperture is given at  
 164 an altitude  $h_{min}$  considering opposite LGSs and neglecting cone effect:

$$h_{min} = \frac{d}{4\alpha}, \quad (1)$$

165 where  $d$  is the size of a sub-aperture and  $\alpha$  is the LGS asterism radius. For MAORY,  $\alpha=45\text{arcsec}$ ,  
 166 and HARMONI,  $\alpha=34\text{arcsec}$ , considering a sub-aperture size of 50cm, this value is 573 and 737m  
 167 respectively, close to M4 conjugation altitude (620m). Instead, the altitude at which opposite LGS  
 168 patch separates at zenith,  $h_{max}$ , is:

$$h_{max} = \frac{Dh_{Na}}{D + \alpha h_{Na}}, \quad (2)$$

169 where  $D$  is the telescope diameter and  $h_{Na}$  is the average sodium altitude. This means that a  
 170 significant part of the turbulence volume is sensed at higher resolution that the one given by the  
 171 sub-aperture size. Still the lower part of the ground layer sensing is limited by the sub-aperture  
 172 size, unless mis-alignments between WFSs sub-aperture grids and pupil is voluntarily introduced.  
 173 This is the strategy followed, and refered to as Geometrical Super Resolution (GSR).

174 An example of Super Resolution is illustrated in Figure 2 where the eigen value of the inter-  
 175 action matrix of a system composed by a  $41 \times 41$  actuator DM and 4 WFS have been plotted for  
 176 various cases :

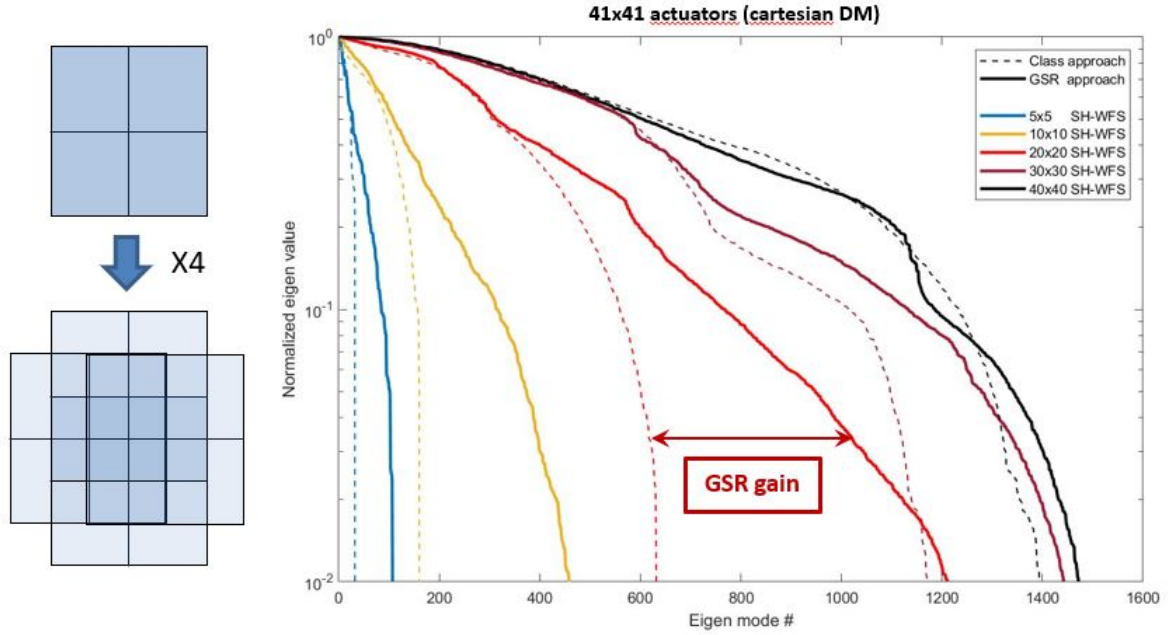


**Fig 2** Impact on eigen values of the GSR with respect to the classical case for configuration with different numbers of sub-apertures. A  $41 \times 41$  actuator DM is considered here. On the left the effect of GSR for a WFS with  $2 \times 2$  sub-aperture is shown.

- 177 • a “classical case” for which the 4 WFS are aligned and see the DM exactly in the same way  
 178 (it corresponds to a classical single WFS system but we keep the 4 WFS in order to keep  
 179 the same number of measurements and normalisation for all the cases). It corresponds to the  
 180 dashed lines in Figure 2
- 181 • a GSR case for which each WFS are shifted by half a sub-aperture in x and y. It corresponds  
 182 to the solid lines in Figure 2

183 for both the classical and the GSR case we consider a WFS with a various number of sub-apertures  
 184 (from  $5 \times 5$  to  $40 \times 40$ , corresponding to various colors in Figure 2) knowing that the reconstruction  
 185 basis remains the same (the  $41 \times 41$  DM actuator basis for all the cases).

186 Figure 2 clearly show the potential of the GSR for the undersampled cases with a significant  
 187 gain in terms of eigen modes with non-null eigen values in comparison to the classical cases. In  
 188 particular it is shown that we have access to typically the same number of modes with a  $30 \times 30$   
 189 WFS with GSR than with a  $40 \times 40$  with a classical approach. Even though the eigen values are  
 190 slightly lower for  $30 \times 30$  with GSR than  $40 \times 40$  with classical approach, the quadratic sum of the  
 191 eigen value only show a 15% decrease and therefore should not bring any significant degradation  
 192 in terms of noise propagation.

193 The application of super-resolution for MAORY is shown in Fig. 3. Here it is interesting to note  
 194 that error increase expected from fitting error, shown in red, is following the law  $k_f \sqrt{d^{5/3} - d_0^{5/3}}$ ,  
 195 while the one found for super-resolution is following the law  $k_s(d - d_0)$ , where  $k_f=194$ ,  $k_s=248$  and  
 196  $d_0=0.4875$ . We verified that all the tested configurations are able to properly correct the turbulence  
 197 with all degrees of freedom of M4 so the error reported above is not sensible to fitting. Moreover  
 198 working in high flux conditions we consider that measurement noise error is negligible. Hence, we

199 hypothesize that the difference in performance is mainly due to spatial aliasing and tomographic error.  
 200 In particular for the tomographic error super-resolution is valid only where the LGS beams  
 201 are super-imposed and when the altitude increases the external part of the meta-pupil covered by  
 202 single beams or the part where the overlap of the beams is partial also increases as can be seen in  
 203 Fig. 4.

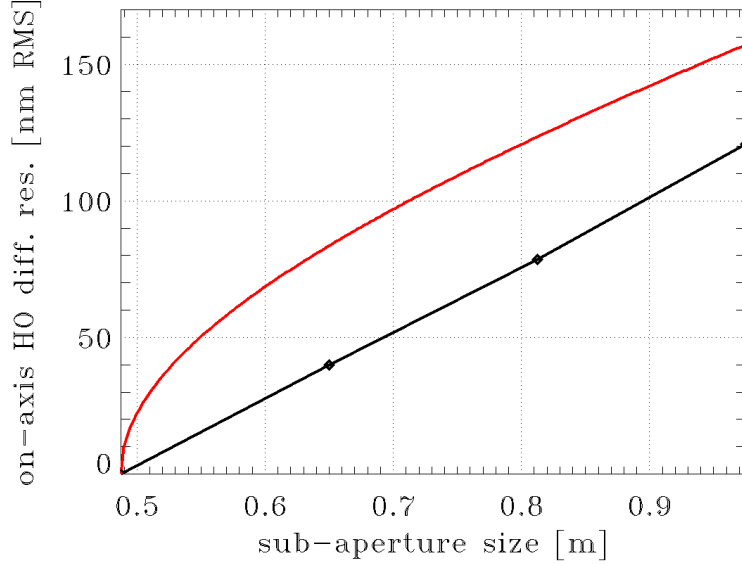


**Fig 3** On-axis MAORY High Order (excluding tilts) differential (with respect to a sub-aperture size of 0.4875m) residual as a function of sub-aperture size. High flux, no elongation. Red line, theoretical residual considering fitting error increase due to lower sampling. Black line is lower thanks to naturally induced super-resolution.

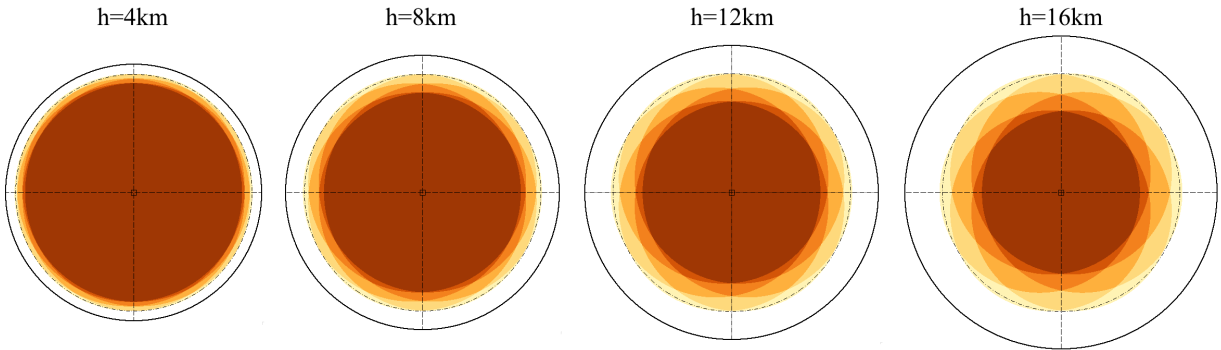


**Fig 4** LGS beams overlap at different altitudes for MAORY working at a zenith angle of 30deg. Decreasing color luminance is used to show an increasing number of overlapping beams. Dotted circle correspond to the pupil size, 39m, while white portion correspond to area where the FoV is not sensed and mainly correspond to technical FoV.

204 The results for the HARMONI case are illustrated in Fig. 5.

205 The residual phase of the “classical case” increases with a slope equal to  $d/r_0^{5/6}$  ( $d$  is the  
 206 sub-aperture size) being limited by the fitting error like a SCAO system. Instead, when super-  
 207 resolution is introduced, following the features listed in Section 3, the slope decreases until with  
 208 GSR it becomes almost flat in the range 100-60 sub-apertures ( $d=0.400-0.667$ m).

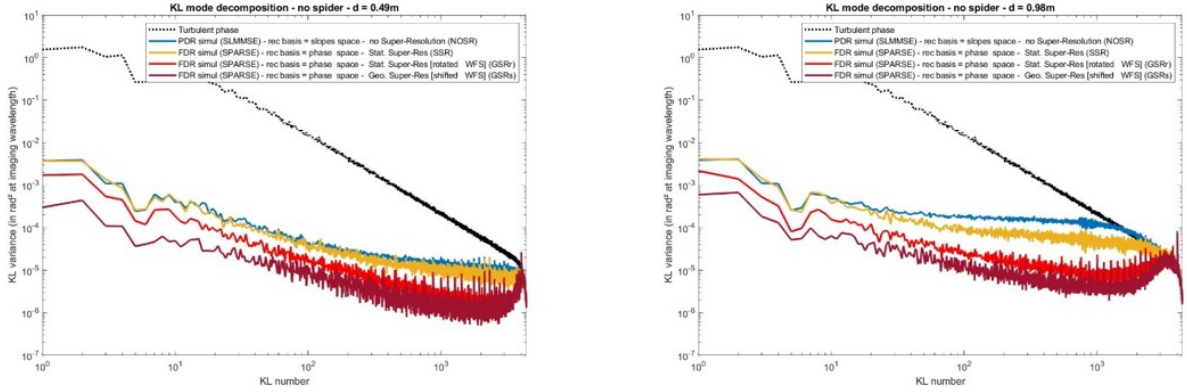
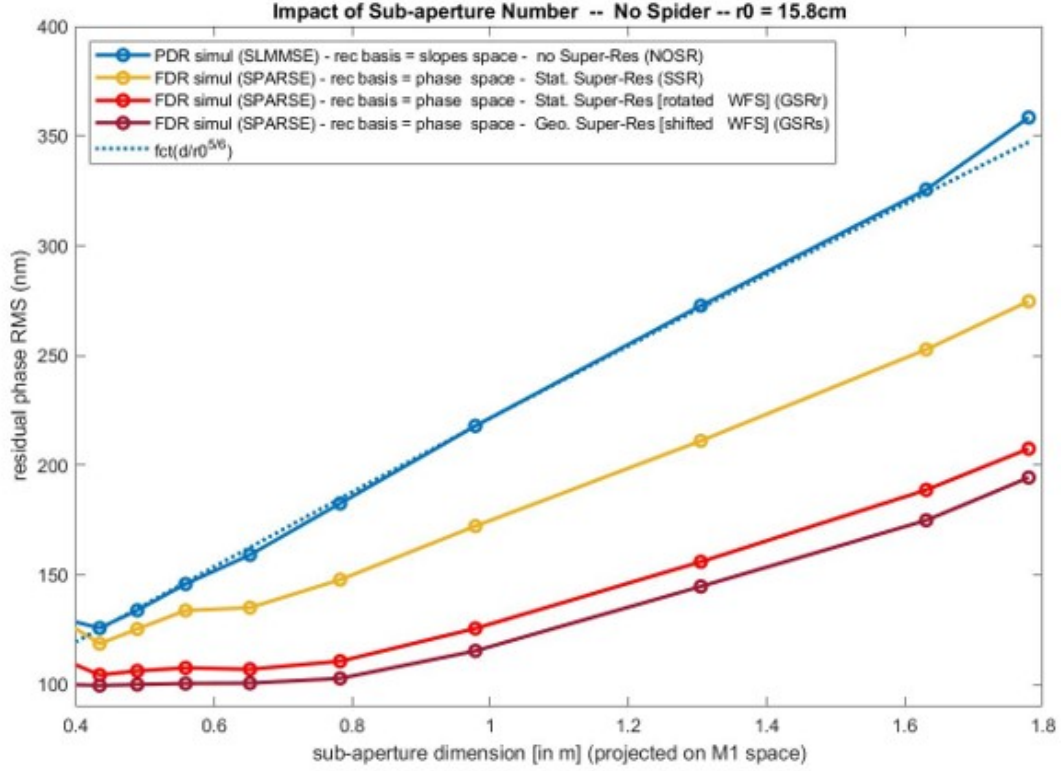


**Fig 5** Impact on performance of sub-aperture size. [Top] residual phase RMS as a function of the sub-aperture dimension - [Bottom] turbulence and residual variance modal decomposition on a Karhunen-Loève base for different configurations for respectively 0.49m (80 sub-apertures in the diameter) and 0.96m (40 sub-apertures in the diameter).for each plot, [blue line] stands for classical AO, orange line for SSR only, [red line] stands for GSR with rotation only between WF and [dark-red line] stands for shift between WFS. Note that a sub-aperture of 0.4m correspond to the case of 100 sub-apertures on the diameter, while 1.8m to 22 sub-apertures.

## 209 4 LGS sampling vs. spot truncation

### 210 4.1 LGS spot size and sampling

211 The sampling impacts both the LGSWFS linearity and noise propagation. For the former, as soon  
 212 as one considers a sampling lower than Shannon (2 pixels per FWHM), an optical gain will appear.

213 For the LGS, this optical gain (conversion between CoG in pixel, and CoG in arcsec) will be  
 214 different for X and Y, and different for each subapertures. This gain changes with seeing, and  
 215 monitoring it requires complex calibration procedures. The extreme example are WFSs working  
 216 with quadcells, and it has been shown that in this case it could represent an important performance  
 217 limiting factor (e.g. GeMS). But Shannon sampling may become very expensive in terms of pixels  
 218 required by the LGWFS, and undersampling the LGS spots may be required. The impact of LGS  
 219 spot undersampling on the centroiding performance has been studied in previous papers (Gratadour  
 220 et al.,<sup>23</sup> Nicolle et al.<sup>24</sup> and Ke, Pedreros et al. this review), and is not detailed here. The conclusion  
 221 (coherent between all the papers) is that one can go down to 1 pixel per FWHM while keeping the  
 222 final error to a reasonable level.

#### 223 4.2 LGS spot truncation

224 The second big problem when dealing with LGS for an ELT comes from the spot elongation. Spot  
 225 elongation per se may not be a problem, as long as enough photons are available to perform cen-  
 226 troiding. The main issue comes from spot truncation, as this introduces biases in the tomographic  
 227 reconstruction. Biases which may be evolving quickly, at a rate following the Sodium layer spatial  
 228 evolution. So truncation and associated biases should be minimized as much as possible. This is  
 229 made possible by (i) maximising the FoV per sub-aperture and (ii) using a regularized reconstruc-  
 230 tion.

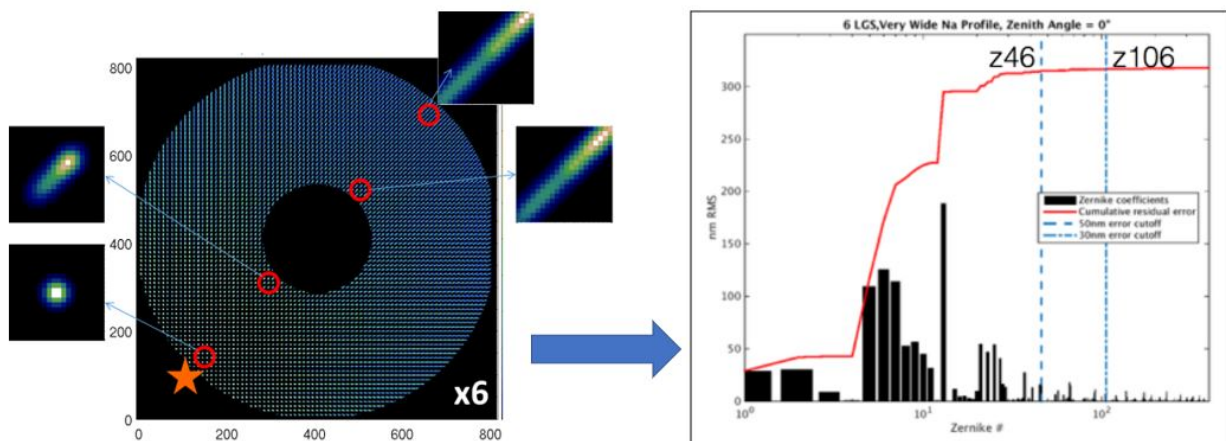


**Fig 6** Example of spot truncation in the extreme case of a very extended sodium profile and a small ( $10'' \times 10''$ ) FoV WFS. [Left] One WFS image, [Right] the aberrations produced by the spot truncation on the 6 LGS after propagation through the tomographic reconstructor

231 Of course these aberrations are static for a given profile but sodium profiles can evolve quite  
 232 rapidly (with timescale of a few seconds typically) and more important, when mixed with tur-  
 233 bulence these effects are randomized and become quite difficult to handle with a dedicated truth  
 234 sensor. The best solutions from a system point of view are therefore twofold

- 235 • to increase the Shack-Hartman sub-aperture FoV in order to reduce the truncation effect at  
 236 its root

237 • add a numerical over-regularisation process (8.25) to over-penalize the signal coming from  
 238 the most truncated in the reconstruction process

239 We have evaluated the impact of the sub-aperture FoV, and spot truncation on performance in  
 240 Figure 7. As can be seen from Figure 7, the truncation error can become very significant when the  
 241 FoV decreases down to 10arcsec. A reasonable FoV per sub-aperture would be to accomodate at  
 242 least 15 to 16arcsec.

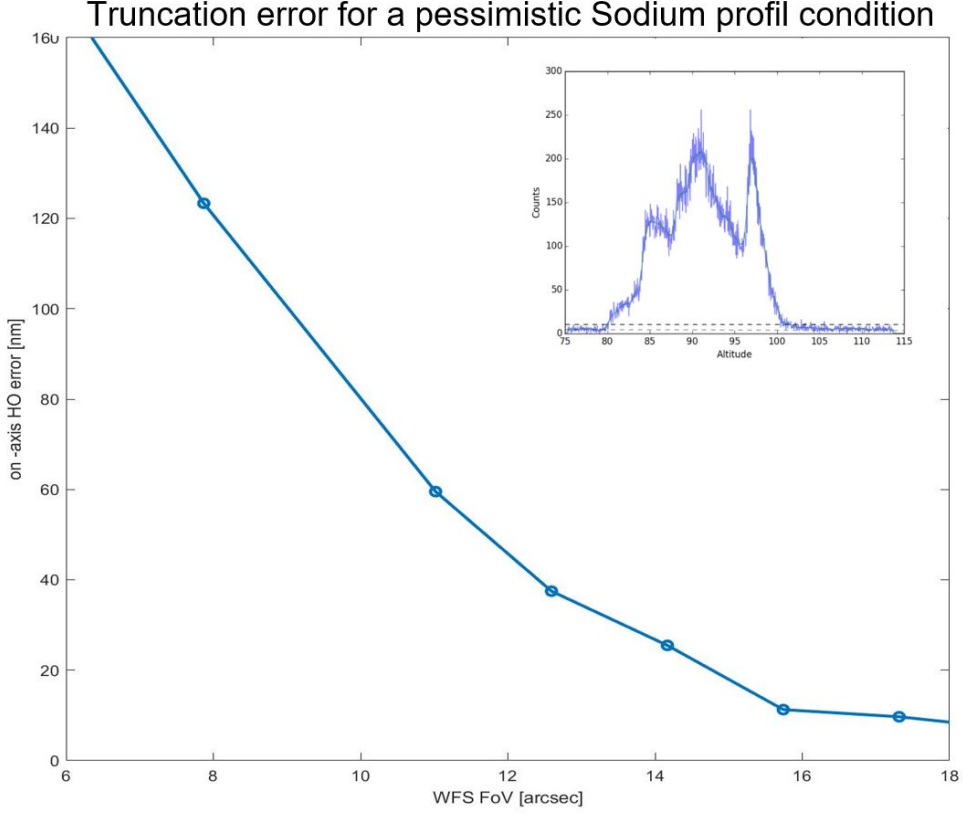


**Fig 7** On-axis High Order (excluding tilts) differential (with respect to a FoV of 22 arcsec) residual as a function of WFS FoV. 68×68 sub-apertures “Very-wide” sodium profile. Sodium profile structure is given at Zenith, the simulation have been made for a 30° zenith angle with the according stretch of the profile altitude. For this particular profile the width is estimated to 22km

## 243 5 Noise propagation

244 The last parameter that must be taken into account for the design of the LGSWFSs for the ELT is  
 245 the sensitivity to noise, both photon and detector noises. We recall that for classical AO system,  
 246 the final noise contribution :  $\sigma_{noise}^2$  can be approximated by the following equation:

$$\sigma_{noise,i}^2 = \sigma_{WFS,\lambda_{wfs}}^2 \left( \frac{\lambda_{wfs}}{\lambda_{im}} \right)^2 * P_{rec,i} * T_{filtering} \quad (3)$$

247 And the propagated noise by:

$$\sigma_{noise,prop}^2 = \sum_{i=1}^{n_{corr}} \sigma_{noise,i}^2 \quad (4)$$

248 where  $\sigma_{WFS,\lambda_{wfs}}^2$  is the variance of the noise at the WFS level,  $\lambda_{wfs}$  is the WFSensing wavelength,  
 249  $\lambda_{im}$  is the imaging wavelength,  $P_{rec,i}$  is the coefficient that takes into account the propagation of  
 250 noise in the phase reconstruction process and  $T_{filtering}$  is the coefficient that takes into account the  
 251 propagation of noise in the temporal filtering process. If we assume that statistically all the WFS  
 252 sub-apertures have the same noise propagation, then we can write:

$$\sigma_{noise,prop}^2 = \sigma_{WFS,\lambda_{wfs}}^2 * \left( \frac{\lambda_{wfs}}{\lambda_{im}} \right)^2 * T_{filtering} \sum_{i=1}^{n_{corr}} P_{rec,i} \quad (5)$$

253  $T_{filtering}$  mainly depend on the temporal aspect of the AO loop : integration time, read-out  
 254 time, control law characteristics and loop delay. For a basic (and yet widely used) integrator-like  
 255 scheme, assuming a 2 frames delay and a loop gain of 0.5 gives  $T_{filtering} 1/10$

256 The main differences between Laser tomographic and classical AO are the following

- 257 •  $\sigma_{WFS,\lambda_{wfs}}^2$  is no more the same for all the sub-aperture and will depend on the spot elongation
- 258 •  $P_{rec,i}$  will include a tomographic reconstruction and will differ from a classical modal basis  
 259 noise propagation matrix as described in Ref. 12 for example.

260 An interesting case to study here is the following: a  $N_{lgs}$  LGS system, without elongation,  
 261 associated to a tomographic case where all the turbulence will be located in the telescope pupil.  
 262 In that particular case,  $P_{recLTAO,i} = \frac{1}{N_{lgs}} P_{rec,SCAO,i}$  and  $\sigma_{WFS,\lambda_{wfs}}^2$  is the same for all the sub-  
 263 apertures of all the LGS. The tomographic noise propagation is therefore nothing but  $\frac{1}{N_{lgs}}$  the  
 264 SCAO noise propagation

265 This limit case allows us to draw the ultimate limits in terms of performance for any wave-front  
 266 sensing configurations. It will also help to understand the influence of the critical parameters of  
 267 the WFS design to be adjusted in final design choice.

268 Let us first study the impact of the main WFS parameters in the ultimate case of photon noise  
 269 limited detector. For that we study the influence of two main parameters : the spot FWHM (mainly  
 270 produced by the combination of the M2 size of the Laser and its propagation through the atmo-  
 271 sphere) and the pixel size (projected on sky).

272 For the photon noise limited case, considering a simple centre of Gravity [CoG], the analytical  
 273 expression of  $\sigma_{WFS,\lambda_{wfs}}^2$  can be expressed as follow

$$\sigma_{ph,\lambda_{wfs}}^2 = \frac{\pi^2}{2 \ln(2)} \frac{1}{N_{ph}} \left( \frac{\sqrt{\text{FWHM}_{spot}^2 + \text{FWHM}_{pixel}^2}}{\text{FWHM}_{diff}} \right)^2 \quad [\text{in rad}^2 \text{ at } \lambda_{wfs}] \quad (6)$$

274 where  $\text{FWHM}_{diff}^2$  is the diffraction limited size of the sub-aperture,  $\text{FWHM}_{spot}$  the FWHM of the  
 275 spot size in the sub-aperture focal plane and  $\text{FWHM}_{pixel}$  the pixel response. Note that for this last  
 276 we have assumed that the pixel FWHM is equal to the physical size of the pixel projected on sky.  
 277 This is not always the case but it remains a fairly good approximation for classical detectors used  
 278 in AO. More importantly, the previous equation is highlighting two fundamental points for a SH :

- 279 • the pixel size of the WFS has to be smaller than the spot size in order to have a negligible  
 280 impact on the noise propagation;

281 • we can defined a “Number of useful photon”  $N_{usefull}$  as

$$N_{usefull} = N_{ph} \left( \frac{FWHM_{diff}}{\sqrt{FWHM_{spot}^2 + FWHM_{pixel}^2}} \right)^2 \quad (7)$$

282 in other words, enlarging the spot or working with large pixel is equivalent to reducing the  
 283 WFS efficiency. As an example, working with 1” pixel combined with 1” FWHM spot is  
 284 2.25 times more efficient than a 1.5” pixel and 1.5 FWHM spot !

285 In the case of uniform Gaussian noise induced by the detector read out (a.k.a. RON), the  
 286 number of pixels becomes a critical parameter. Again, considering a classical CoG, the analytical  
 287 expression of the measurement variance is

$$\sigma_{ron, \lambda_{wfs}}^2 = \frac{\pi^2}{3} \left( \frac{FWHM_{pixel}}{FWHM_{diff}} \right)^2 \left( \frac{ron}{N_{ph}} \right)^2 \left( \frac{N_s}{N_d} \right)^2 \quad [\text{in rad}^2 \text{ at } \lambda_{wfs}] \quad (8)$$

288 with  $\frac{FWHM_{pixel}}{FWHM_{diff}}$  convert pixel error in radian.  $ron$  stands for the read-out noise,  $N_s$  stands for the  
 289 total number of pixel involved in the CoG computation and  $N_d$  the number of pixel in the spot  
 290 FWHM. Assuming that  $N_s$  is computing as the ratio of a spot era equal to 2 times the spot FWHM  
 291 and the pixel size,  $\frac{N_s}{N_d} = 4 * \frac{FWHM_{spot}}{FWHM_{pixel}}$  as soon as  $FWHM_{pixel} < FWHM_{spot}$  and  $\frac{N_s}{N_d} = 4$  otherwise.

$$\sigma_{ron, \lambda_{wfs}}^2 = \frac{\pi^2}{3} \left( \frac{FWHM_{pixel}}{FWHM_{diff}} \right)^2 \left( \frac{ron}{N_{ph}} \right)^2 \left( 4 * \frac{FWHM_{spot}}{FWHM_{pixel}} \right)^2 \quad [\text{in rad}^2 \text{ at } \lambda_{wfs}] \quad (9)$$

293 And finally the ron contribution to WFS measurement variance can be approximated by

$$\sigma_{ron, \lambda_{wfs}}^2 = \frac{16\pi^2}{3} \left( \frac{ron}{N_{ph}} \right)^2 \left( \frac{FWHM_{spot}}{FWHM_{diff}} \right)^2 \quad \text{if } FWHM_{spot} > FWHM_{pixel} \quad (10)$$

$$= \frac{16\pi^2}{3} \left( \frac{ron}{N_{ph}} \right)^2 \left( \frac{FWHM_{pixel}}{FWHM_{diff}} \right)^2 \quad \text{if } FWHM_{spot} < FWHM_{pixel} \quad (11)$$

294 Here again it is very easy to understand the importance of the spot FWHM and of the pixel size  
 295 in the noise produced by any SH measurement. It is essential to minimize these two parameters in  
 296 order to have the smallest possible noise and keep the pixel size close (but slightly smaller) than  
 297 the spot FWHM.

298 Although it is quite easy to develop analytical formulae under the hypothesis of a single WFS  
 299 and symmetric and identical (statistically speaking) spot shape for all the sub-aperture. In the case  
 300 of a tomographic AO system none of these hypothesis remains true. We have multiple LGS and  
 301 variable elongation in the sub-apertures. If the tendencies highlighted by the theoretical develop-  
 302 ments remain correct, it is important to have a full simulation in order to have a better understanding  
 303 of the limitations and behaviour in a full LTAO case. Using full end-to-end simulation but looking  
 304 at the noise propagation term only, we have estimated the performance sensitivity to photon and  
 305 RON noise. This is illustrated by Figure 8.

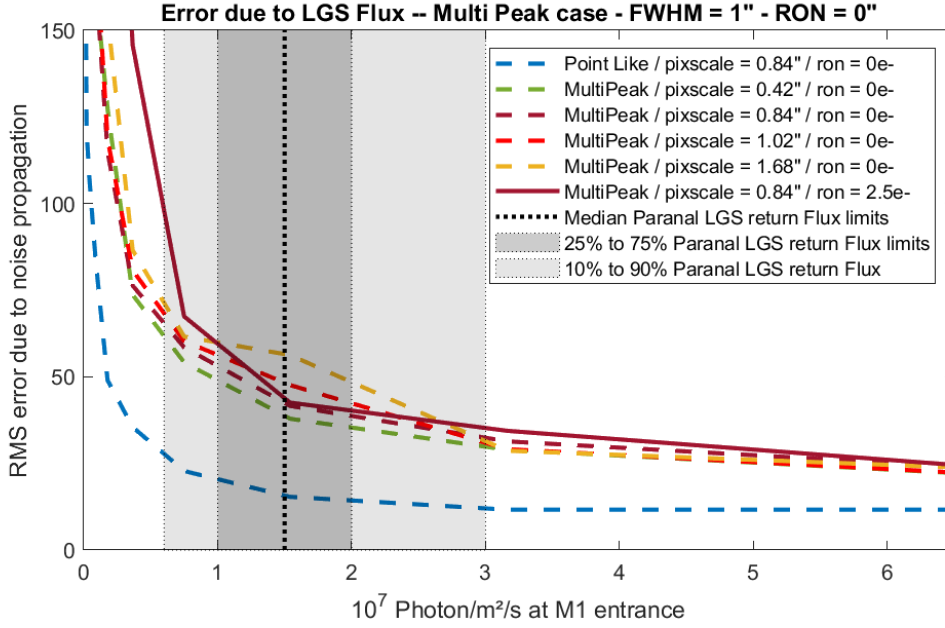


**Fig 8** Impact of sodium return flux on performance. Error RMS as a function of the sodium return flux for point like and “multi-peak”<sup>26</sup> sodium profile and different pixel scales.

306 Several conclusions can be derived from this figure

- 307 • for ELT application and scaling flux returns measured after more than 4 years of LGS operation at Paranal with AOF, the noise error terms for extended spot (we have considered here  
308 some extreme case of Sodium profile) remains quite reasonable : around 50nm rms  
309
- 310 • the very first increase of noise is due to the spot elongation. For photon noise only, going  
311 from a Point link source to an extended LGS increases the noise from 15 to 41 nm rms, that  
312 is an quadratic increase of 38 nm rms
- 313 • the pixel size (as shown in Eq 6) is also an important parameter. In the photon limited case  
314 its increase by a factor 4 (from 0.42 to 1.68'') has led additional noise error of 40 nm rms  
315 (quadratic increase). In other word a factor 4 of sampling increase on noise propagation has  
316 the same impact than the spot elongation itself.
- 317 • adding Read-Out-Noise has a dramatic impact for low flux cases. In the typical range of  
318 return flux we will have to consider with the ELT and considering RON smaller than 3e-,  
319 the impact remains very small. Note that we have considered here a very basic 3 $\sigma$  threshold  
320 algorithm for the centroiding measurements. A more clever approach (Weighted Center of  
321 Gravity, Correlation or Match Filter) will further reduced the impact.

322 In conclusion, with an end-to-end simulation and looking at the noise propagation error term  
323 only, we have shown that noise propagation error remains quite low for a LTAO system working  
324 with Paranal typical flux return. The RON is not a major contributor if it remains smaller than  
325 3 e-. Pixel scales have to remain reasonably small with a good (not to say optimal) compromise  
326 around the typical size of the spot small axis FWHM (that is around 1'').

## 327 **6 Potential LGSWFS designs**

328 In the previous sections we have derived the performance sensitivity to several factors, like the  
329 pupil spatial sampling, LGS spot sampling and impact of truncation. In this section, we have  
330 now to put these sensitivity analyses in front of expected LGS parameters, and eventually provide  
331 recommendations on what a LGSWFS should be for the ELT. This should not be seen as a design  
332 definition, but guidelines for tomographic AO systems for the ELT. Of course, LGSWFS design  
333 choices strongly depends on the Sodium characteristics, so we begin this section by an overview  
334 of typical Sodium parameter distribution derived from the VLT operation.

### 335 *6.1 Sodium typical characteristics*

336 The Adaptive Optics Facility (AOF<sup>27</sup>) has been operational on the UT4 telescope at Paranal since  
337 2017, providing access to a deformable secondary mirror (DSM) and four LGS units (4LGSF)  
338 for a variety of instruments. The GALACSI AO module is also part of the modules delivered  
339 within the AOF, bringing AO correction capabilities for the MUSE instrument, and is also a great  
340 tool to gather statistics on the Na layer characteristics thanks to the continuous logging of the AO  
341 telemetry data.

342 The LGS spot size on sky is dependent of the seeing but also on the laser launch telescope  
343 design. During the 4LGSF design phase, a full end-to-end simulation has been conducted, consid-  
344 ering the 30-cm launch diameter, uplink and downlink propagation (with cone effect), to evaluate  
345 the spot size and verify compliance with specifications. The simulation values were confirmed  
346 with on-sky measurements during the commissioning phase, with a FWHM of 1.05'' for the small  
347 axis and 1.61'' for the long axis, with the atmosphere seeing being 0.6'' and UT4 pointing altitude  
348 of 60 degrees. Measurements were also taken at different pointing altitudes showing no significant  
349 dependence, and with different seeing conditions. With a seeing of 1'', the measured spot size was  
350 about 1.35'' for the small axis and 2.1'' for the long axis. These spot sizes were measured on the  
351 UT4 guiding camera for the full 8-m aperture and with the LGS in the center of the field.

352 During on-sky operation of GALACSI, the fluxes of all four WFSs are logged regularly. Data  
353 are available since July 2017 and are processed to derive the statistics of returned flux, converted  
354 to photons per second and per m<sup>2</sup> at M1 entrance. The first parameter impacting the flux return is  
355 the pointing direction of the telescope at the time of the observation.<sup>28</sup> Fig.9 presents the sky plot  
356 of the simulated LGS flux return for a seeing of 0.8'', a sodium abundance of  $4 \times 10^{13}$  atoms/m<sup>2</sup>,  
357 and a 20W class laser at Paranal, showing the high variability of the return flux versus the pointing  
358 direction.

359 The second parameter affecting the LGS flux return is the Na column abundance, which varies  
360 with time, on both long- and short-time scales. The Na column abundance in atoms/m<sup>2</sup> can be  
361 retrieved from the return flux measured on GALACSI, by correcting for the effect of the point-  
362 ing direction. Fig.10 shows the statistics of the Na column abundance per month. The "violin"  
363 representation shows the distribution of the Na column abundance from all the measurements of  
364 each month. The median value is shown as a red dot. The months when too few measurements  
365 were obtained to be statistically relevant have been marked with a 0. The known seasonal cyclic  
366 variation between the summer (low return) and winter (high return) months can be seen on the  
367 measurements. Differences can also be seen from year to year in the global average. Atmosphere  
368 studies show a link between the Na abundance and the Sun activity cycle of 11 years.<sup>29</sup> The last

369 peak of the Sun activity was in 2014, with a decrease since that date. The prediction for the Sun  
 370 activity show a minimum in 2021 and the start of a new cycle with the next peak in 2025.

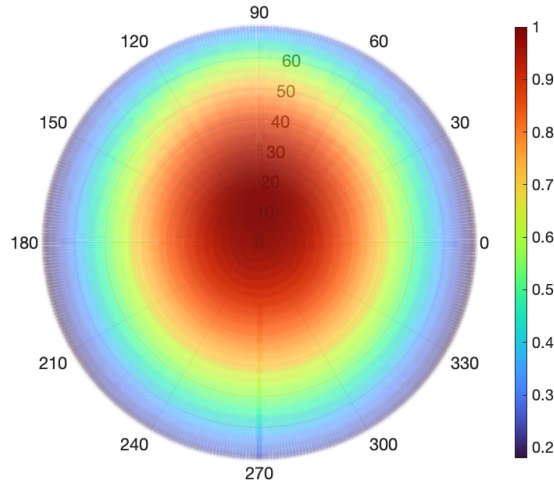


**Fig 9** Sky plot of the theoretical LGS flux return at Paranal for a seeing of 0.8'', normalized to the maximum value, based on the LGSBloch model (N=90, E=0).

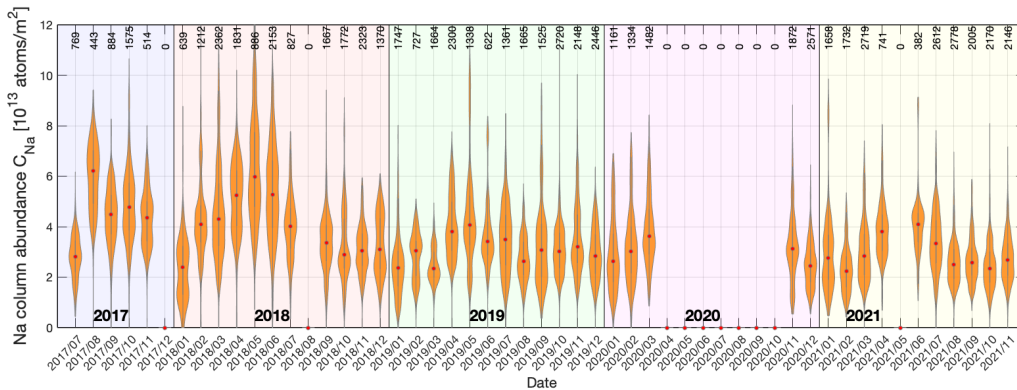


**Fig 10** Statistics of Na column abundance per month.

371 The morphology and temporal variations of the Na layer has been studied with different meth-  
 372 ods and at different sites.<sup>26,30,31</sup> No measurements of this type exist for the VLT or ELT, but the  
 373 three studies reported similar results for very different location on Earth and their results can thus  
 374 be considered representative for the ELT also. The following parameters can thus be used to de-  
 375 scribe the general structure of the Na layer, with all altitude given above sea level: mean centroid  
 376 altitude of  $90.8 \pm 0.1$  km, altitude range (containing 95% of the photons) of  $13.1 \pm 0.3$  km (minimum  
 377 width of 6 km a maximum one of 21 km), mean lower edge altitude of  $81.7 \pm 0.1$  km, mean upper  
 378 edge altitude of  $104.9 \pm 0.3$  km.

379 The mean altitude also shows variations at the level of the night. The power spectral density  
 380 of these variations can be represented by a power law:  $P_a(\nu) = \alpha \nu^\beta$ , with  $\nu$  the fluctuations

381 frequency. The amplitude  $\alpha$  and power coefficient  $\beta$  show variations from night to night, but can  
 382 be represented by the following mean values:  $\alpha = 34.4_{-4.8}^{+5.6} m^2 Hz^{-1}$  and  $\beta = -1.87 \pm 0.02$ .

383 The Na density vertical structure is also showing a high variability, and it is considered difficult  
 384 to define any kind of typical vertical profile. An attempt has still been made at classifying the zoo  
 385 of profiles measured on-sky into seven different classes.<sup>26</sup>

## 386 6.2 Toward LGSWFS for the ELT

387 In this section, and based on the Sodium inputs derived above, we evaluate the boundary condi-  
 388 tions recommended for the main LGSWFS parameters for the ELT, which are the number of sub-  
 389 apertures (pupil sampling), the field-of-view per sub-aperture and the pixel scale. Of course, hidden  
 390 behind this trade-off are the detectors characteristics, which are the number of pixels, the frame  
 391 rate, and the Read-Out Noise (RON). Depending on the detector availability and performance, one  
 392 can adjust the LGSWFS parameters to fit into a given detector format, and the sensitivity study  
 393 presented here allows that. Here we have provided boundaries for the LGSWFS parameters which  
 394 allow to optimize the performance, assuming that suitable detectors are available (e.g. Ke, Pe-  
 395 dreros et al. this review). These trade-offs are summarized in Table 1. Basically, and based on the  
 396 trade-off between pupil sampling, LGS spot truncation and LGS spot sampling, the recommenda-  
 397 tion for the ELT would be to deploy LGSWFSs with  $>64 \times 64$  subapertures,  $>16$ arcsec FoV and  
 398 a pixel scale  $<1.15$ arcsec. Deviating from these basic parameters would increase the overall error  
 399 budget. A practical implementation based on these numbers is described in Ke, Pedreros et al.  
 400 (this review).

**Table 1** LGSWFS main parameters for an ELT (40m) telescope

Parameters	range	Comments
subaps	$>64^2$	See Fig. 5. Use of super resolution allows to use less subapertures than DM actuators, but the larger the sampling, the better the performance. Going down to $64 \times 64$ has negligible impact on the performance.
FoV	$>16^2$ arcsec <sup>2</sup>	See Fig. 7. The larger the FoV, the better the performance. Going above 16arcsec allows to minimize the truncation error for the worst Na profiles
Pixel Scale	$<1.15$ arcsec	This is set by the minimum expected LGS spot size, and to maintain a good sampling and a decent noise propagation (see Fig. 8) .
RON	$<3 e-$	with a good target around $2.5 e-$ . This value is fixed to be almost photon noise limited in the typical range of LGS flux return (see Fig. 8)

## 401 7 Conclusion

402 In this paper we have explored the key LGSWFS parameters impacting the performance when  
 403 deployed at the ELT scale. When going from the current generation of 8-10m telescopes to a 40m  
 404 scale, the first challenge comes from the LGS spot elongation. Where it only represents a few  
 405 arcseconds for 8-10m telescope, it becomes a major limitation for ELT, with expected elongations  
 406 of up to 25arcsec. Designing an LGSWFS then becomes a challenge, as one has to manage both  
 407 the FoV and the small axis sampling. As this is out of reach of current detector technologies, a  
 408 trade-off has to be made. In this paper, we open a new dimension in this trade-off, but making use  
 409 of the so-called super resolution, and by taking advantage of the fact that we have several LGSWFS

410 looking at an almost similar turbulence volume. Combining the signal from the multiple WFSs,  
411 we show that we can go beyond the historical paradigm of matching the subapertures count with  
412 the DM actuators geometry. Thanks to super resolution, we show that fewer subapertures per WFS  
413 can be used, which opens the path for realistic LGSWFS designs.

#### 414 *Acknowledgments*

415 This work benefited from the support the following grants: WOLF ANR-18-CE31-0018, F-CELT  
416 ANR-21-ESRE-0008 and LabEx FOCUS ANR-11-LABX-0013 of the French National Research  
417 Agency (ANR), OPTICON H2020 (2017-2020) Work Package 1 (Calibration and test tools for AO  
418 assisted E-ELT instruments) grant number 730890, Action Spécifique Haute Résolution Angulaire  
419 (ASHRA) of CNRS/INSU co-funded by CNES.

#### 420 *References*

- 421 1 R. Tamai, B. Koehler, M. Cirasuolo, *et al.*, “The ESO’s ELT construction progress,” in *Soci-*  
422 *ety of Photo-Optical Instrumentation Engineers (SPIE) Conference Series, Society of Photo-*  
423 *Optical Instrumentation Engineers (SPIE) Conference Series* **11445**, 114451E (2020).
- 424 2 E. Vernet, M. Cirasuolo, M. Cayrel, *et al.*, “ELT M4 — The Largest Adaptive Mirror Ever  
425 Built,” *The Messenger* **178**, 3–4 (2019).
- 426 3 R. Ragazzoni, “Pupil plane wavefront sensing with an oscillating prism,” *Journal of Modern*  
427 *Optics* **43**, 289–293 (1996).
- 428 4 R. Ragazzoni, D. Greggio, V. Viotto, *et al.*, “Extending the pyramid WFS to LGSs: the  
429 INGOT WFS,” in *Adaptive Optics Systems VI*, L. M. Close, L. Schreiber, and D. Schmidt,  
430 Eds., *Society of Photo-Optical Instrumentation Engineers (SPIE) Conference Series* **10703**,  
431 107033Y (2018).
- 432 5 S. Esposito, G. Agapito, C. Giordano, *et al.*, “Pyramid wavefront sensing using Laser Guide  
433 Star for 8m and ELT class telescopes,” in *Adaptive Optics Systems V*, E. Marchetti, L. M.  
434 Close, and J.-P. Véran, Eds., *Society of Photo-Optical Instrumentation Engineers (SPIE)*  
435 *Conference Series* **9909**, 99096B (2016).
- 436 6 C. Arcidiacono, S. Di Filippo, D. Greggio, *et al.*, “Ingot wavefront sensor: from the Fourier  
437 End2End numerical simulation to the LOOPS test bench,” in *Society of Photo-Optical In-*  
438 *strumentation Engineers (SPIE) Conference Series, Society of Photo-Optical Instrumentation*  
439 *Engineers (SPIE) Conference Series* **11448**, 1144868 (2020).
- 440 7 E. Gendron, “Optical solutions for accommodating ELT LGS wave-front sensing to small  
441 format detectors,” in *Adaptive Optics Systems V*, E. Marchetti, L. M. Close, and J.-P. Véran,  
442 Eds., *Society of Photo-Optical Instrumentation Engineers (SPIE) Conference Series* **9909**,  
443 99095Z (2016).
- 444 8 S. Oberti, C. Vérinaud, M. Le Louarn, *et al.*, “LGS tomography and spot truncation: tips and  
445 tricks,” in *6th International Conference on Adaptive Optics for Extremely Large Telescopes,*  
446 *AO4ELT 2019*, (Québec, Canada) (2019).
- 447 9 L. Bardou, É. Gendron, G. Rousset, *et al.*, “ELT-scale elongated LGS wavefront sensing:  
448 on-sky results,” *A&A* **649**, A158 (2021).

- 449 10 P. Ciliegi, G. Agapito, M. Aliverti, *et al.*, “MAORY: the adaptive optics module for the  
450 Extremely Large Telescope (ELT),” in *Society of Photo-Optical Instrumentation Engineers*  
451 *(SPIE) Conference Series, Society of Photo-Optical Instrumentation Engineers (SPIE) Con-*  
452 *ference Series* **11448**, 114480Y (2020).
- 453 11 N. A. Thatte, I. Bryson, F. Clarke, *et al.*, “HARMONI: first light spectroscopy for the ELT: in-  
454 strument final design and quantitative performance predictions,” in *Society of Photo-Optical*  
455 *Instrumentation Engineers (SPIE) Conference Series, Society of Photo-Optical Instrumenta-*  
456 *tion Engineers (SPIE) Conference Series* **11447**, 114471W (2020).
- 457 12 F. Rigaut and E. Gendron, “Laser guide star in adaptive optics: the tilt determination prob-  
458 lem.,” *A&A* **261**, 677–684 (1992).
- 459 13 D. L. Fried and J. F. Belsher, “Analysis of fundamental limits to artificial-guide-star adaptive-  
460 optics-system performance for astronomical imaging.,” *Journal of the Optical Society of*  
461 *America A* **11**, 277–287 (1994).
- 462 14 C. Béchet, M. Le Louarn, R. Clare, *et al.*, “Closed-loop ground layer adaptive optics simula-  
463 tions with elongated spots : impact of modeling noise correlations,” in *Adaptive Optics for*  
464 *Extremely Large Telescopes*, 03004 (2010).
- 465 15 J.-P. Véran and G. Herriot, “Centroid gain compensation in ShackHartmann adaptive optics  
466 systems with natural or laser guide star,” *Journal of the Optical Society of America A* **17**,  
467 1430–1439 (2000).
- 468 16 M. A. van Dam, “Measuring the centroid gain of a shack–hartmann quad-cell wavefront  
469 sensor by using slope discrepancy,” *J. Opt. Soc. Am. A* **22**, 1509–1514 (2005).
- 470 17 B. Neichel, F. Rigaut, F. Vidal, *et al.*, “Gemini multiconjugate adaptive optics system re-  
471 view - II. Commissioning, operation and overall performance,” *Monthly Notices of the Royal*  
472 *Astronomical Society* **440**, 1002–1019 (2014).
- 473 18 J. M. Beckers, “Adaptive Optics for Astronomy: Principles, Performance, and Applications,”  
474 *Annual Review of Astronomy and Astrophysics* **31**, 13–62 (1993).
- 475 19 M. Sarazin, M. Le Louarn, J. Ascenso, *et al.*, “Defining reference turbulence profiles for E-  
476 ELT AO performance simulations,” in *Proceedings of the Third AO4ELT Conference*, S. Es-  
477 posito and L. Fini, Eds., 89 (2013).
- 478 20 L. Busoni, G. Agapito, C. Plantet, *et al.*, “Adaptive optics design status of MAORY, the  
479 MCAO system of European ELT,” in *6th International Conference on Adaptive Optics for*  
480 *Extremely Large Telescopes, AO4ELT 2019*, (Québec, Canada) (2019).
- 481 21 S. Oberti, M. Le Louarn, E. Diolaiti, *et al.*, “MAORY design trade-off study: tomography  
482 dimensioning,” in *Adaptive Optics for Extremely Large Telescopes*, (2017).
- 483 22 S. Oberti, P. Guiraud, C. Correia, *et al.*, “Super-resolution Wavefront Reconstruction,” *As-*  
484 *tronomy & Astrophysics, Submitted* .
- 485 23 D. Gratadour, E. Gendron, T. Fusco, *et al.*, “Comparing centroiding methods for Shack-  
486 Hartmann wavefront sensing with laser guide stars on an ELT,” in *Adaptive Optics Systems*  
487 *II*, B. L. Ellerbroek, M. Hart, N. Hubin, *et al.*, Eds., *Society of Photo-Optical Instrumentation*  
488 *Engineers (SPIE) Conference Series* **7736**, 77361A (2010).
- 489 24 M. Nicolle, T. Fusco, G. Rousset, *et al.*, “Improvement of Shack-Hartmann wave-front sensor  
490 measurement for extreme adaptive optics,” *Optics Letters* **29**, 2743–2745 (2004).
- 491 25 T. Fusco, B. Neichel, C. Correia, *et al.*, “A story of errors and bias: The optimization of the  
492 LGS WFS for HARMONI,” in *AO4ELT6*, (Quebec City, Canada) (2019).

- 493 26 T. Pfrommer and P. Hickson, “High resolution mesospheric sodium properties for adaptive  
494 optics applications,” *Astronomy & Astrophysics* **565**, A102 (2014).
- 495 27 R. Arsenault, P. Y. Madec, J. Paufique, *et al.*, “Progress on the VLT Adaptive Optics Facility,”  
496 *The Messenger* **142**, 12–16 (2010).
- 497 28 R. Holzlöhner, S. M. Rochester, T. Pfrommer, *et al.*, “Laser guide star return flux simulations  
498 based on observed sodium density profiles,” in *Adaptive Optics Systems II*, B. L. Ellerbroek,  
499 M. Hart, N. Hubin, *et al.*, Eds., *Society of Photo-Optical Instrumentation Engineers (SPIE)*  
500 *Conference Series* **7736**, 77360V (2010).
- 501 29 D. M. Simonich, B. R. Clemesha, and V. W. J. H. Kirchhoff, “The mesospheric sodium layer  
502 at 23°S: Nocturnal and seasonal variations,” *Journal of Geophysical Research* **84**, 1543–1550  
503 (1979).
- 504 30 J. Castro-Almazan, A. Alonso, D. Bonaccini Calia, *et al.*, “Na LGS height profiles at Teide  
505 Observatory, Canary Islands,” in *5th International Conference on Adaptive Optics for Ex-*  
506 *tremely Large Telescopes, AO4ELT 2017*, (Tenerife, Canary Islands, Spain) (2017).
- 507 31 B. Neichel, C. D’Orgeville, J. Callingham, *et al.*, “Characterization of the sodium layer at  
508 cerro pachon, and impact on laser guide star performance,” *Monthly Notices of the Royal*  
509 *Astronomical Society* **429** (2013).